













Extraction of Gamow-Teller strengths in the β^+ direction with the $(d, {}^2\text{He})$ reaction in inverse kinematics

Z. Rahman ^{1,2,3,*} S. Giraud^{1,2,†} J. C. Zamora ¹ R. G. T. Zegers ^{1,2,3,‡} Y. Ayyad ¹ S. Beceiro-Novo ^{3,4}
 D. Bazin ^{1,3} B. A. Brown ^{1,2,3} A. Carls^{1,2,3} J. Chen^{1,5} M. Cortesi ¹ M. DeNudt^{1,2,3} C. Maher^{1,2,3}
 W. Mittig^{1,3} F. Ndayisabye¹ S. Noji ¹ J. Pereira^{1,2} J. Schmitt^{1,2,3} M. Z. Serikow ^{1,3}
 L. J. Sun ^{1,2} J. Surbrook^{1,2,3} N. Watwood ^{1,2,3} and T. Wheeler^{1,2,3}

¹*Facility for Rare Isotope Beams, Michigan State University, East Lansing, Michigan 48824, USA*

²*Joint Institute for Nuclear Astrophysics: Center for the Evolution of the Elements, Michigan State University, East Lansing, Michigan 48824, USA*

³*Department of Physics and Astronomy, Michigan State University, East Lansing, Michigan 48824, USA*

⁴*Universidad da Coruña, Campus Industrial de Ferrol, CITENI, Departamento de Física, Ferrol 15403, Spain*

⁵*Physics Division, Argonne National Laboratory, Lemont, Illinois 60439, USA*



(Received 19 June 2024; accepted 30 July 2024; published 14 August 2024)

The $(d, {}^2\text{He})$ reaction in inverse kinematics has been developed for experiments with rare-isotope beams to constrain electron-capture rates needed for astrophysical simulations of processes in dense nuclear environments such as supernovae and neutron star crusts. The first experiment focused on the measurement of the ${}^{14}\text{O}(d, {}^2\text{He})$ and ${}^{13}\text{N}(d, {}^2\text{He})$ reactions in inverse kinematics, utilizing the active-target time-projection chamber placed in front of the S800 magnetic spectrograph. This work focuses on the experimental and analysis details, and presents the results for the ${}^{13}\text{N}(d, {}^2\text{He})$ reaction, which is important for constraining electron capture rates on ${}^{13}\text{N}$ in the preexplosion convective phase of Type Ia supernova. The extracted Gamow-Teller transition strengths associated with electron capture on ${}^{13}\text{N}$ are consistent with those previously obtained from the analog transitions from ${}^{13}\text{C}$. The successful development of the $(d, {}^2\text{He})$ reaction in inverse kinematics presents a novel opportunity for performing experiments aimed at constraining electron-capture rates in nuclei far from stability.

DOI: [10.1103/PhysRevC.110.024313](https://doi.org/10.1103/PhysRevC.110.024313)

I. INTRODUCTION

Electron captures (ECs) on nuclei play a key role in a variety of stellar phenomena, such as core-collapse and thermonuclear supernovae, crustal processes of accreting neutron stars, and the late evolution of intermediate-mass stars [1–10]. Allowed Gamow-Teller (GT) transitions, associated with no change in angular momentum ($\Delta L = 0$), a change in spin ($\Delta S = 1$), and a change in isospin ($\Delta T = 1$), dominate the EC rates, unless temperatures and densities are very high and forbidden transitions also contribute [2,3,10–12]. Stellar EC rates are different from terrestrial EC rates as a result of the high densities and high temperatures in astrophysical environments. At high temperatures, ECs will occur from excited states in the parent nucleus. At high density and Fermi energy, EC to states at high excitation energy will occur. In addition, many isotope species, including unstable ones, will play a role in the astrophysical environments. Therefore, theoretical modeling is crucial for making estimates of EC rates. These theoretical models need to be benchmarked against experimental data where available, and improved when

necessary. Direct measurement of GT transition strengths [$B(\text{GT})$] through EC/ β -decay data is only possible for transitions from ground state (g.s.) to g.s. or low-lying states due to the limitations imposed by the Q value. Charge-exchange (CE) reactions are employed to study transitions to excited states as they connect the same initial and final states as weak-interaction processes, but do not have the Q -value limitation. Charge-exchange reactions at intermediate energies ($E \gtrsim 100$ MeV/nucleon) can be used to extract the $B(\text{GT})$ indirectly based on a well-established proportionality relationship between $B(\text{GT})$ and the CE differential cross section at zero momentum transfer [13]:

$$\frac{d\sigma}{d\Omega}(q=0) = \hat{\sigma}_{\sigma\tau} B(\text{GT}), \quad (1)$$

where $\hat{\sigma}_{\sigma\tau}$ is the unit cross section, which is calibrated by using transitions for which the $B(\text{GT})$ is known from direct measurements.

CE experiments in the EC/ β^+ direction that probe proton-hole, neutron-particle excitations are necessary for constraining stellar EC rates. As mentioned above, many of the nuclei involved in the relevant astrophysical scenarios are unstable. Therefore, CE experiments in inverse kinematics, in which the unstable isotope of interest is the beam, are necessary. However, such experiments are challenging. A suitable neutron target for an (n, p) experiment is not available.

*Contact author: rahman@frib.msu.edu

†Contact author: giraud@frib.msu.edu

‡Contact author: zegers@frib.msu.edu

In inverse-kinematics reactions with light ions at $q \approx 0$, the ejectile is emitted with very low kinetic energy and is easily stopped or perturbed in the target. To avoid this issue, the (${}^7\text{Li}$, ${}^7\text{Be}$) reaction has been studied in inverse kinematics without the detection of the ${}^7\text{Be}$ ejectile [14,15]. However, because the ${}^7\text{Be}$ ejectile is not detected, measurements through this method have been limited to lighter nuclei and excitation energies up to particle separation.

The (d , ${}^2\text{He}$) reaction has been used successfully in the past for studying CE reactions on stable nuclei in forward kinematics in experiments at the RIKEN Accelerator Facility [16–18], Texas A&M University Cyclotron Institute [19], and the Kernfysisch Versnellend Instituut (KVI) [20]. An extensive program aimed at extracting GT strengths for astrophysical purposes and for constraining matrix elements for double β decay was carried out with the EuroSupernovae detector system stationed at the Big Bite Spectrometer at KVI, see, e.g., Refs. [20–27]. Based on the successes of those experiments, the (d , ${}^2\text{He}$) reaction in inverse kinematics was studied in this work as a probe for extracting GT strengths in the EC/ β^+ direction from unstable nuclei. A cocktail beam comprising of ${}^{14}\text{O}$, ${}^{13}\text{N}$, and ${}^{12}\text{C}$ was used in the experiment. The results for the ${}^{14}\text{O}(d, {}^2\text{He})$ reaction in inverse kinematics have been published in Ref. [28]. These results demonstrated that coupled-cluster calculations successfully reproduced the experimental GT $^+$ strength distribution. Notably, this was achieved without using a phenomenological quenching factor, which is typically necessary to gain consistency between shell-model calculations and experimental data. In this paper, the details of the new method are discussed and the results from the ${}^{13}\text{N}(d, {}^2\text{He})$ reaction are presented.

In the deuteron g.s., a proton and neutron are predominantly coupled in a ${}^3\text{S}_1$ configuration with a small ${}^3\text{D}_0$ component. If the relative energy ϵ_{pp} between the two protons in the two-proton system is small, it primarily has a ${}^1\text{S}_0$ configuration, which is referred to as the ${}^2\text{He}$ particle. In the ${}^1\text{S}_0$ configuration, the (d , ${}^2\text{He}$) reaction proceeds with the transfer of spin ($\Delta S = 1$), which is beneficial for isolating and identifying GT transitions. The (d , ${}^2\text{He}$) experiments in forward kinematics described above primarily focused on selecting events with $\epsilon_{pp} \lesssim 1\text{--}2$ MeV. The dominance of the $\Delta S = 1$ transfer is approximately valid for ($\epsilon_{pp} \lesssim 4$ MeV) [29].

The transitions from the ${}^{13}\text{N}(1/2^-)$ g.s. to the ${}^{13}\text{C}(1/2^-)$ g.s. and the ${}^{13}\text{C}(3/2^-)$ excited state at 3.68 MeV are important for the preexplosion convective phase in Type Ia supernova [30,31]. The transition strengths from the ${}^{13}\text{N}$ g.s. to ${}^{13}\text{C}$ g.s. was determined using the literature value of $\log ft$ from β^+ decay [32]. However, determining the transition strength to the 3.68 MeV excited state from β^+ decay was not possible, as this transition is energetically forbidden. The shell-model code OXBASH [33] predicts $B(\text{GT}) = 1.52$ for this transition by using the CKII interaction [34] in the p -shell-model space, after taking into account a well-known quenching factor qf^2 of 0.68, calculated with the phenomenological relation established for nuclei in the p shell [35]:

$$qf = 1 - 0.19 \left(\frac{A}{16} \right)^{0.35}. \quad (2)$$

As discussed in Ref. [31], the shell-model calculations with the CKII interaction are similar, but a little closer to the experimental values from β decay from those calculated with the WBT interaction [36,37], hence we have used the CKII interaction in this work.

Several experiments using (p , n) [13,36,38,39] and (${}^3\text{He}$, t) [31,40] reactions have been used to study the analog transition from ${}^{13}\text{C}$ g.s. to the ${}^{13}\text{N}$ excited state at 3.51 MeV. From these, one can determine the strength for the transitions from the ${}^{13}\text{N}$ to the ${}^{13}\text{C}$ at 3.68 MeV assuming isospin symmetry. In principle, one can use the known transition strength from β decay from the ${}^{13}\text{N}$ g.s. to calibrate the unit cross section, but that transition is of mixed GT and Fermi nature, which introduces a systematic uncertainty since the contribution from the Fermi component needs to be subtracted. In the (p , n) experiments, the extracted GT strengths for the transition to the state at 3.51 MeV were significantly lower than predicted in the shell model: 0.82 ± 0.05 [38] and 1.06 ± 0.05 [36].

To avoid systematic uncertainties in the determination of the GT unit cross section associated with the subtraction of the Fermi contribution to the g.s. of ${}^{13}\text{N}$, in the analysis based on (${}^3\text{He}$, t) [31,40] data, the unit cross section was calibrated by using the transition to the ${}^{13}\text{C}(3/2^-, T = 3/2)$ state at 15.1 MeV. For this transition, the GT strength (0.23 ± 0.01) can be deduced from the analog β -decay transitions from the g.s. of ${}^{13}\text{B}$ to the g.s. of ${}^{13}\text{C}$ and from the g.s. of ${}^{13}\text{O}$ to the g.s. of ${}^{13}\text{N}$ [13,31]. As a result, the GT transition strength to the 3.51-MeV state was deduced to be 1.37 ± 0.07 , much closer to the shell-model results. In this work, the GT strengths for transitions contributing to the EC on ${}^{13}\text{N}$ were measured directly, including to the 3.68-MeV state in ${}^{13}\text{C}$. Although the statistical uncertainties are too large to improve on the accuracy of the extracted strengths from the ${}^{13}\text{C}({}^3\text{He}, t)$ experiments [31,40], we show that the results are consistent with that data.

The organization of this paper is as follows. Section II presents the experimental details, Sec. III details the data analysis, Sec. IV presents the results and discussion, and Sec. V presents the summary and outlook. Simulations that were used in the analysis of experimental data (for this paper and Ref. [28]) have been detailed in Ref. [41].

II. EXPERIMENTAL DETAILS

A cocktail beam of ${}^{14}\text{O}$ (105 MeV/nucleon), ${}^{13}\text{N}$ (94 MeV/nucleon), and ${}^{12}\text{C}$ (81 MeV/nucleon) was produced from the fragmentation of a primary ${}^{16}\text{O}$ beam at 150 MeV/nucleon accelerated by the Coupled Cyclotron Facility at NSCL. A 1316 mg/cm 2 thick Be production target was used. A 150 mg/cm 2 thick Al degrader was used in the A1900 fragment separator [42] to purify the cocktail beam consisting of 70% ${}^{14}\text{O}$, 23% ${}^{13}\text{N}$, and 7% ${}^{12}\text{C}$. Beam intensities between 100 kpps and 700 kpps were used for this experiment.

The beam from the A1900 was sent to the S800 spectrograph. The time-of-flight (ToF) between the two scintillators placed at the exit of A1900 separator and the entrance of the beam line towards the S800 spectrograph [43] was used to separate the different components in the beam. The distance between the two scintillators was 25.3 m. Figure 1 shows an

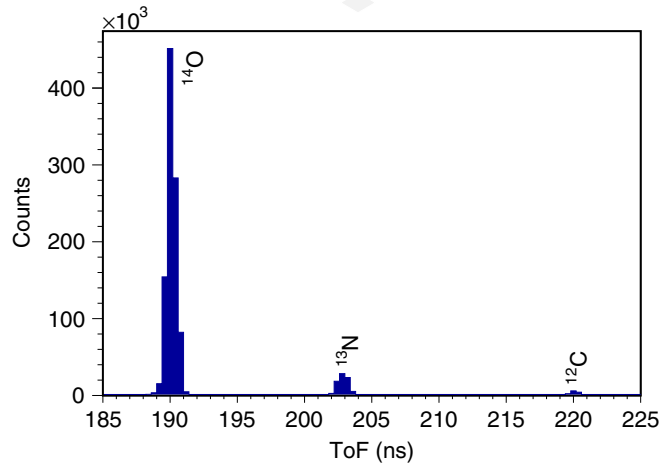


FIG. 1. ToF (in ns) between the two scintillators placed at the exit of A1900 separator and the entrance of the beam line to the S800 spectrograph, illustrating the event-by-event particle identification of the incoming beam particles. The data shown are from the runs for which the S800 spectrograph was set at a magnetic rigidity of $B\rho = 3.0582$ Tm.

example of the incoming beam particle identification (PID) during the runs for which magnetic rigidity ($B\rho$) of the S800 was 3.0582 Tm. Since this spectrum was gated on events in which a particle that reacted in the target was detected in the S800 focal-plane detector system, the contributions from the different beam components in the cocktail beam are different from the fractions listed above.

The active target-time projection chamber [44] (AT-TPC) was used at the target location of the S800 spectrograph. The AT-TPC has a cylindrical geometry with a 52 cm diameter and an active length of 100 cm along the beam direction. For this experiment, it was filled with deuterium gas at a pressure of 530 Torr, corresponding to a target thickness of 11.7 mg/cm². The gas serves as the detector medium and the target, enabling the measurement of nuclear reactions with large solid angles and low detection-energy thresholds.

The incoming beam enters the AT-TPC through a window in the upstream flange, inducing a reaction while traveling along the symmetry axis. The reaction product exits through a window in the downstream flange and was then magnetically analyzed in the S800 spectrograph. Polyamide windows with a thickness of 12 μ m separate the AT-TPC gas volume from the beam line and spectrograph vacuum. A 500 V/cm uniform electric field is applied parallel to the beam axis inside the AT-TPC. The charged particles involved in the nuclear reactions ionize the gas, producing electron-ion pairs along their trajectories in the active volume. The electrons drift toward the micromegas detector composed of 10240 pads, located at the upstream end of the AT-TPC. The pad plane and the cathode plane at the downstream end of the AT-TPC have holes with a diameter of 3 and 4 cm, respectively, to allow the beam to enter and exit the AT-TPC. The pad signals are transmitted to the AsAd (ASIC support and analog to digital conversion) boards and then to concentration boards, which generate a time stamp for correlating the AT-TPC events with

the corresponding S800 events. The x and y coordinates of the tracks are reconstructed based on the position of the activated pad. The z coordinate is extracted from the drift time of the electrons in the gas and their velocity. The drift time was measured relative to the timing provided by the focal-plane scintillator of the S800 spectrograph. The drift velocity was determined to be ≈ 0.9 cm/ μ s. Because of the holes in the pad and cathode planes, the central region of the AT-TPC volume is insensitive and the beam intensity can be relatively high.

The beamlike particles were transmitted through the AT-TPC to the S800 spectrograph. Because of the central insensitive region, tracks from the beam particles, fast reaction products, and their decay particles were not detected in the AT-TPC. At the focal plane [45] of the S800 spectrograph, two cathode readout drift chambers (CRDCs) measured the position and angle of the fragments. Additionally, the energy-loss measurement in an ionization chamber provided an indirect measurement of the atomic number of the fragments. A plastic scintillator gave a timing signal that was used for PID and for triggering the data acquisition system.

Three different $B\rho$ settings, centered around $B\rho$ values of 2.8384 Tm, 3.0582 Tm, and 3.2705 Tm, were chosen to cover the $B\rho$ windows associated with the production of ¹⁴N through the ¹⁴O(d , ²He) reaction, as well as the population of ¹³N, ¹³C, and ¹²C following the deexcitation of ¹⁴N by the emission of a neutron, a proton, or a proton and a neutron, respectively. These three $B\rho$ windows are illustrated in Fig. 2(a). The decay by proton and/or neutron emission resulted in a broadening of the momentum or $B\rho$ distribution of the particle detected in the S800. This is illustrated in Fig. 2(b), in which the measured $B\rho$ distributions of ¹⁴N and ¹²C particles are shown. Both were detected in the same central $B\rho$ setting for the S800 spectrograph. Whereas the distribution for ¹⁴N was narrow, the emission of a neutron and a proton broadened the distribution for ¹²C.

As shown in Fig. 2(a), the $B\rho$ settings optimized for the detection of the ¹⁴O(d , ²He) reaction products also allowed for the detection of reaction products from the ¹³N(d , ²He) reaction, although the events associated with the population of ¹²B after the decay by proton emission from ¹³C were outside of the $B\rho$ acceptances. The $B\rho$ acceptance for events associated with the ¹²C(d , ²He) reaction was limited, as illustrated in Fig. 2(a). Since the intensity of the ¹²C beam was low, a meaningful analysis of this reaction was not possible.

III. DATA ANALYSIS

A. Particle identification in the S800 spectrograph

The products from reactions that occurred in the AT-TPC were identified in the S800 spectrograph by using the energy-loss, time-of-flight (ΔE -ToF) method. The ΔE signal was obtained from the ionization chamber, after correction for the weak dependence on momentum and track angle determined from the measurements in the drift chambers. The ToF was determined from the timing measurements in the scintillator placed at the entrance of the S800 beam line and the S800 focal-plane scintillator, also after the correction for the dependence on momentum and track angle. An example

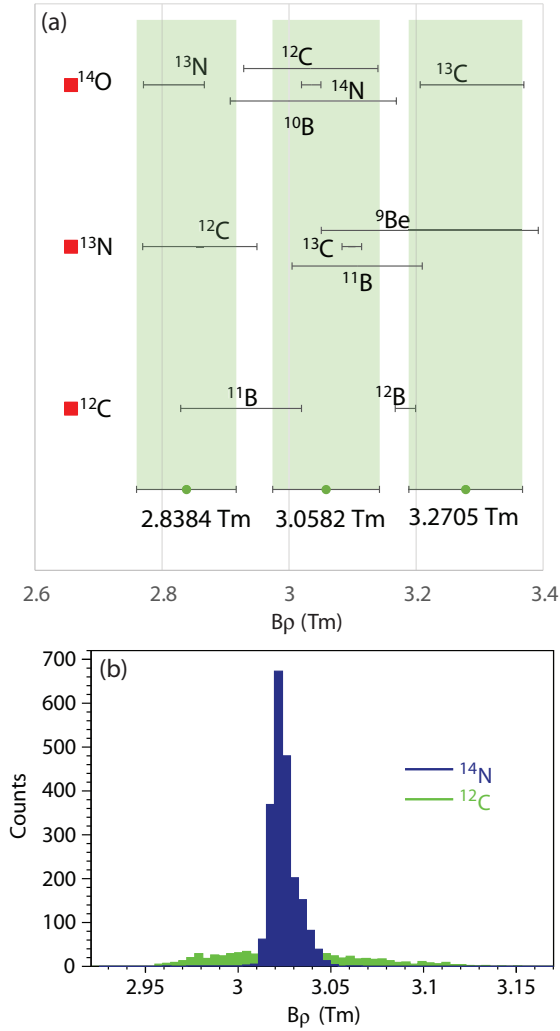


FIG. 2. (a) $B\rho$ ranges of the CE reaction products or their decay products produced in the ($d, ^2\text{He}$) reaction on the ^{14}O , ^{13}N , and ^{12}C isotopes in the cocktail beam. For each of the produced isotopes, the horizontal bars indicate the full width of the $B\rho$ distribution, taking into consideration the momentum kicks induced through the decay by particle emission at the highest excitation energy at which that particle was or could be observed. The bottom row indicates the three $B\rho$ settings used in the experiment. In this case, the horizontal bars and green bands indicate the $B\rho$ acceptance ($\pm 3\%$) for each setting. (b) Measured $B\rho$ distributions of ^{14}N and ^{12}C for the $^{14}\text{O}(d, ^2\text{He})$ reaction, taken at the central $B\rho$ setting of 3.0582 Tm.

PID plot for the case of the central rigidity of 3.0582 Tm is shown in Fig. 3. This PID plot contains reaction products after gating on the incoming ^{13}N in the cocktail beam. The selected events shown in this PID plot originate from various reactions induced by ^{13}N in the deuterium gas in the AT-TPC. By gating on different reaction products, events in which ^2He is identified in the AT-TPC (see below) can be associated with a specific decay channel of ^{13}C produced in the $^{13}\text{N}(d, ^2\text{He})$ reaction. For the example shown in Fig. 3, these include ^{13}C , ^{11}B , and ^9Be . Among other reaction products, the $^{13}\text{N}^{6+}$ can also be identified. It is produced by fully ionized ^{13}N beam particles that pick up an electron in the AT-TPC.

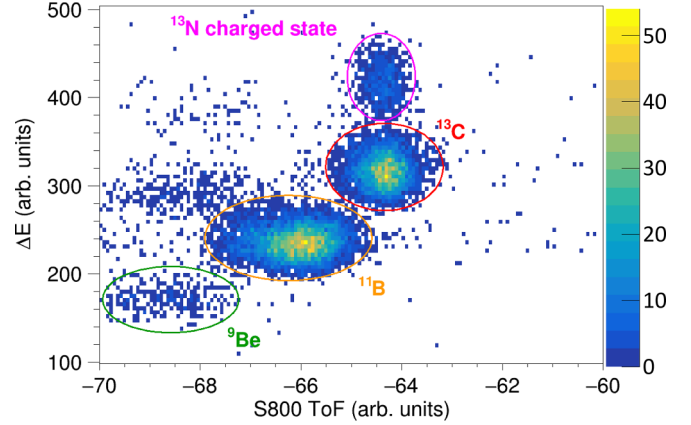


FIG. 3. Particle identification with the S800 spectrograph after gating on events in which the incoming beam particles are identified as ^{13}N .

B. Event reconstruction in the AT-TPC

An event occurring within the gas volume of the AT-TPC generates a point cloud, which is a set of hit points defined by their spatial coordinates. The coordinates of each point in the point cloud were determined as follows. In the directions perpendicular to the beam direction (z axis), the coordinates of the hit points were determined from the hit pattern on the plane of the AT-TPC. In the z direction, the coordinate is determined by the drift length of the electrons, which is calculated from the drift time and the drift velocity. The drift velocity depends on detailed properties of the gas and was found to slightly change over time, presumably due to the presence of trace contaminants in the gas. Therefore, the drift velocity was adjusted on a run-by-run basis by ensuring that the drift length ranged between 0 cm and 100 cm, the physical length of the active volume of the AT-TPC. This is illustrated in Fig. 4. Figure 4(a) shows the drift length distribution in the z direction for 30 data runs of approximately an hour. Before a correction to the drift velocity was applied, the maximum drift length was below 100 cm. After the correction of the velocity, the maximum drift length was 100 cm. Figure 4(b) shows the drift length distributions for two different runs, prior to the correction of the drift velocities. The corrections that needed to be applied were different for the two runs. Finally, Fig. 4(c) shows the maximum drift length as a function of run number before (in red) and after (in blue) the drift-velocity corrections were applied. The corrections applied followed a smooth trend as a function of run number, which strongly correlates with time.

After the run-by-run corrections for the drift velocity, the point clouds obtained in each event were analyzed using a random sample consensus (RANSAC) algorithm. The details of the algorithm as applied to the analysis of AT-TPC data are described in Refs. [46,47]. The primary source of background in the AT-TPC is due to the production of δ electrons. The charges induced on the pad plane by the interaction of δ electrons in the gas is much lower than those due to the protons or other ion tracks. Therefore, the application of a simple threshold was used to effectively remove most of the signals

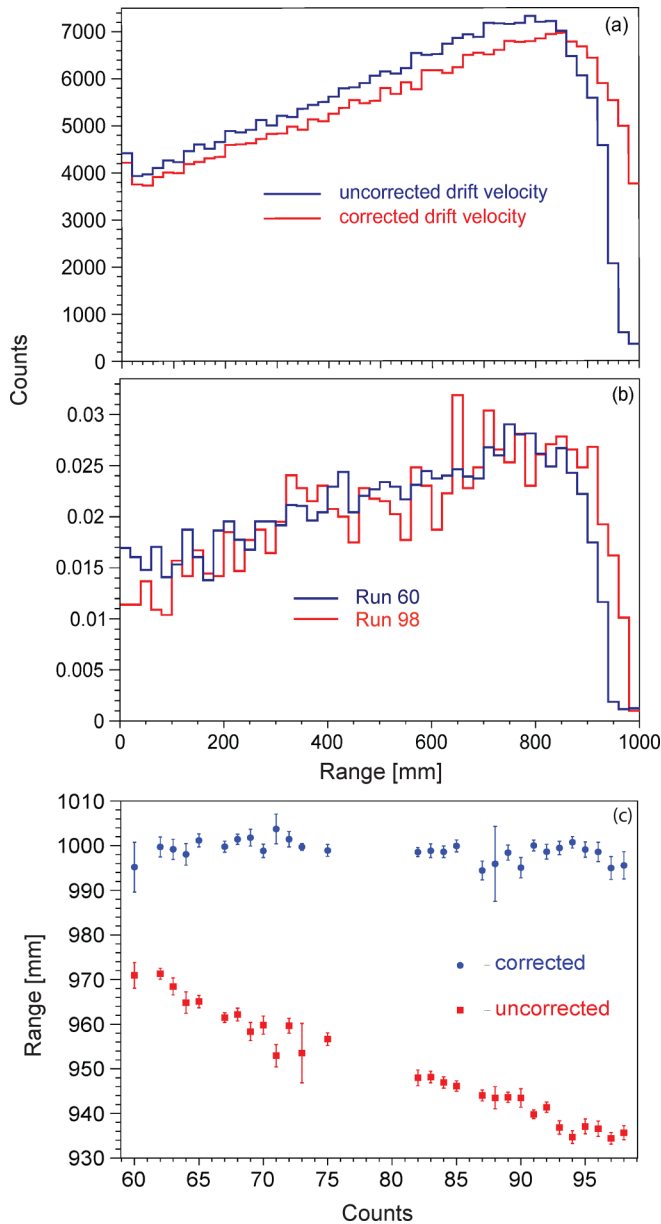


FIG. 4. (a) The drift length distribution for 30 runs before (in blue) and after (in red) drift-velocity correction. (b) Drift-length distributions for two runs before drift-velocity correction, indicating that the correction is run dependent. For comparison, the distributions for both runs are normalized to 1. (c) The maximum drift length all as a function of run number before (red) and after (blue) drift velocity correction. The plotted uncertainties represent the uncertainties in the fit of the maximum drift distance.

caused by the δ electrons. For each of the tracks identified in the algorithm, a three-dimensional line was fitted through a χ^2 minimization process. An example of the result from the RANSAC algorithm for a (d , ^2He) event with fitted tracks is shown in Fig. 5(a). Some isolated signals not belonging to a particular track are also visible. They are due to electronic noise or some remaining signal from δ electrons.

In events where at least two tracks were identified, a vertex was determined by the center of the closest distance between

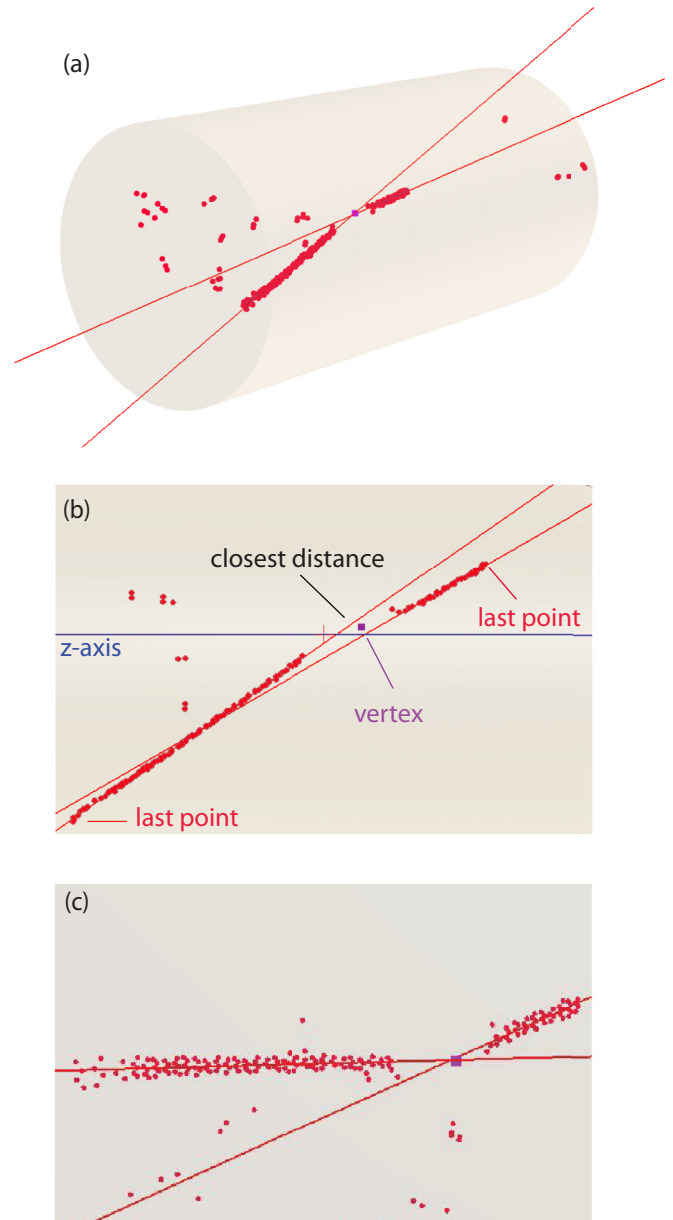


FIG. 5. (a) Example of a (d , ^2He) event in the AT-TPC together with the fitted lines following the RANSAC algorithm. (b) Determination of the closest distance between the two tracks, the vertex location, and the last points of each track for the same events as shown in (a). (c) The same event as in (a) and (b) but from a different perspective.

the two fitted tracks, as shown in Fig. 5(b). Figure 5(c) shows the same event, but from a different perspective. Please note that, because the central region of the AT-TPC was insensitive, the location of the vertex was based on the extrapolated tracks from the fitting process. The determination of the vertex location was weighted by the number of hits in each track if one of the tracks had less than 50 data points. Omitting weighing for tracks with fewer than 50 data points resulted in a wider distribution of the closest distance between the two tracks. The distribution of the closest distance between the two tracks was a half-normal distribution with a scale parameter σ

that varied between 5.0 and 6.3 mm during the experiment. Events with the closest distance between the tracks of more than 2σ , amounting to about 5% of the events, were rejected from the analysis.

The length of each track was then defined as the distance between the position of the vertex and the projection of the last point in the point cloud of the fitted line. In Fig. 5(b), the last points for each of the identified tracks are identified. Events in which one of the tracks did not end within the active volume of the AT-TPC were not included in the remaining analysis. The event loss due to one of the protons stopping within the insensitive region around the beam axis or due to one or both of the tracks exiting from the AT-TPC was corrected for, as discussed below.

As discussed in Ref. [41], it was expected that space-charge effects negatively impact the quality of the track reconstruction, especially near the beam axis. However, since the beam intensities in this experiment were below 10^6 particles per second and the beam had a small atomic number, the effects were observed to be very minor and efforts to correct for space-charge effects did not improve the results.

The axis of the AT-TPC did not align exactly with the beam axis. The beam axis was determined by combining the reconstructed vertices from many events and had an angle of about 1.6° relative to the central axis of the AT-TPC. This offset was taken into account when performing the kinematic event reconstruction discussed below.

The requirement of having two tracks from a single vertex together with the measurement of a relevant reaction product in the focal plane of the S800 spectrograph removes background from the (d , ^2He) CE events. For example, the most likely reaction is elastic scattering off the deuteron, but the elastically scattered particle did not enter the S800 focal plane at rigidity settings for CE events. Still, a single track could be produced [most likely due to (d , d') or (d , p) reactions] that would interfere with a (d , ^2He) event. However, even though the readout window for tracks in the AT-TPC was relatively long ($\approx 110 \mu\text{s}$), at beam intensities of less than 10^6 particles per second, the chance of having a random coincident event within that time window and with a vertex separated by less than 2σ was about $\approx 0.01\%$ of the (d , ^2He) reaction rate and was disregarded [41].

C. Kinematic event reconstruction

For each of the events identified as being due to a (d , ^2He) CE reaction, the energy of each of the protons was determined from their path lengths using an energy-loss look-up table calculated using SRIM [48]. In combination with the track angles, the momentum vectors \mathbf{p}_1 and \mathbf{p}_2 of the protons were reconstructed. From these momentum vectors, the momentum of the ^2He particle $\mathbf{p}_{^2\text{He}}$ was calculated:

$$\mathbf{p}_{^2\text{He}} = \mathbf{p}_1 + \mathbf{p}_2. \quad (3)$$

The mass of the ^2He particle $M_{^2\text{He}}$ was obtained from an invariant-mass calculation:

$$M_{^2\text{He}} = \sqrt{(E_1 + E_2)^2 - (\mathbf{p}_1 + \mathbf{p}_2)^2}, \quad (4)$$

where E_1 and E_2 are the total energies for each of the two protons. The relative energy was calculated from:

$$\epsilon_{pp} = M_{^2\text{He}} - 2M_p, \quad (5)$$

where M_p is the rest mass of the proton. The excitation energy of the CE reaction product (i.e., ^{14}N or ^{13}C) was calculated in a missing-mass calculation. The average values for the energy and angle of the incoming beam particles were used in this calculation, as the incoming momentum vector was not tracked on an event-by-event basis. In this calculation, the average values for the energy and angle of the incoming beam particles were utilized, as the incoming momentum vector was not tracked on an event-by-event basis. These uncertainties, along with those associated with the determination of the momenta of the two protons in the AT-TPC, were the two predominant factors affecting the reconstruction of the excitation energy and the scattering angle.

D. Acceptance corrections

To extract differential cross sections, it was important to correct for the acceptance for detecting the two protons from the ^2He particle and the residual particle in the focal-plane detector system of the S800 spectrograph. To determine the acceptances, the ATTPCROOT simulation package [41,49,50] was used. It consists of three main parts: event generation, digitization, and reconstruction.

Events were generated by using the theoretical cross section obtained from adiabatic coupled-channels Born approximation (ACCBA) code [51], which has been well tested in the analysis of (d , ^2He) experiments performed in forward kinematics. The code is based on a parameter-free method to treat the three-body dynamics of the (d , ^2He) reaction by using the adiabatic approximation and allows for the calculation of the differential cross section as a function of ϵ_{pp} and the center-of-mass scattering angle $\theta_{\text{c.m.}}$, which was important for the acceptance corrections in the present work. As the dynamics of the (d , ^2He) reaction is included without the introduction of free parameters [51], the primary inputs for the code are similar to that of other distorted wave Born approximation codes used for other CE reactions: (i) microscopic one-body transition densities of relevant transitions in the target-residual system, which were calculated in the shell-model code NUSHELLX [52] by using the CKII interaction [34] in the p -shell-model space for the $0\hbar\omega$ transitions. For $1\hbar\omega$ dipole transitions, calculations were performed in the normal-modes formalism [53] by using the code NORMOD [54]; (ii) the effective two-body interaction from the t matrix developed by Love and Franey [55,56]; and (iii) optical potentials for the deuteron-target and residual-proton systems were taken from the Koning-Delaroche phenomenological potential [57], where the extended parametrizations in the code TALYS [58,59] were used.

We refer the reader to Ref. [41] for more details of the simulations performed for the (d , ^2He) reactions in the AT-TPC placed at the S800 spectrograph. The simulation was built to generate digitized data with the same structure as the data measured with the detector. Therefore, the same analysis

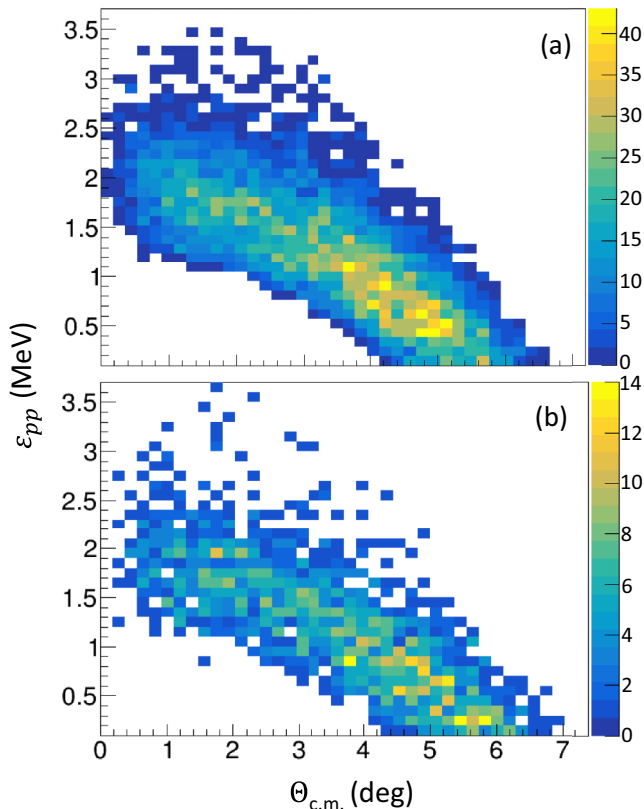


FIG. 6. Correlations between the relative energy ϵ_{pp} and the center-of-mass scattering angle $\theta_{c.m.}$ for the $^{14}\text{O}(d, ^2\text{He})^{14}\text{N}(1^+; 3.95 \text{ MeV})$ reaction inside the sensitive region of AT-TPC as a function of scattering angle for the $^{14}\text{O}(d, ^2\text{He})^{14}\text{N}$ reaction in (a) the simulation and (b) the data.

codes can be used for the simulated and experimental data. This ensures a consistent treatment of acceptances and gates.

To illustrate the importance of the acceptance correction, Fig. 6 shows the comparison between [Fig. 6(a)] the simulated and [Fig. 6(b)] the measured correlations between ϵ_{pp} and $\theta_{c.m.}$ for the $^{14}\text{O}(d, ^2\text{He})^{14}\text{N}(1^+; 3.95 \text{ MeV})$ reaction, which is the strongest transition measured in the experiment. For $\theta_{c.m.} \lesssim 2^\circ$, the momentum transfer to the ^2He system in the $(d, ^2\text{He})$ reaction is small and, if ϵ_{pp} is also small ($\epsilon_{pp} \lesssim 1.2 \text{ MeV}$), one or both of the protons will not make it out of the central insensitive region of the AT-TPC. On the other hand, for the same low scattering angles, one or both of the protons will escape from the AT-TPC if $\epsilon_{pp} \gtrsim 3.0 \text{ MeV}$, and the event is also lost. For $\theta_{c.m.} \gtrsim 4^\circ$, the opposite happens. Since the momentum transfer to the ^2He system is relatively large, only events where $\epsilon_{pp} \lesssim 1.4 \text{ MeV}$ will have one of the protons not escape the AT-TPC and be reconstructible. For intermediate scattering angles, the situation is somewhere in between these two extremes. The correlation between ϵ_{pp} and $\theta_{c.m.}$ obtained in the simulation is consistent with the one observed in the experiment.

The correlation shown in Fig. 6 depends not only on ϵ_{pp} and $\theta_{c.m.}$, but also on the excitation energy of the residual nucleus: (i) a higher excitation energy is associated with a higher momentum transfer to the ^2He system, and (ii) if the

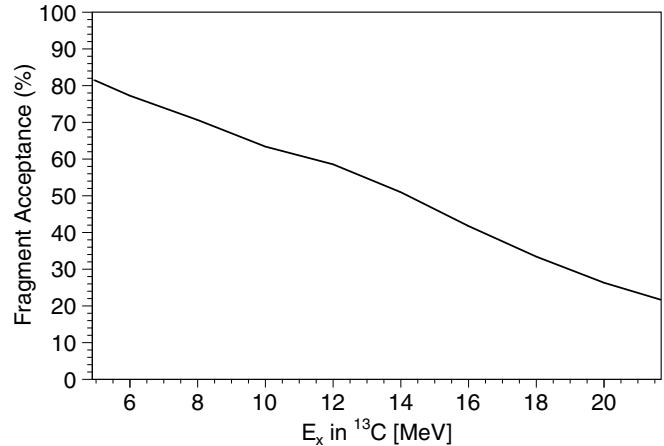


FIG. 7. Simulated fragment acceptance as a function of excitation energy in ^{13}C for events obtained by gating on ^{12}C particle.

excitation energy increases beyond the threshold for decay by particle emission, the momentum induced to the residual particle by the emitted particle(s) broadens the momentum and angular distributions of the residual particles. The broadened distributions could lead to a loss of events due to the limited momentum and angular acceptances of the S800 spectrograph. The broadening of the angular distribution also leads to a loss of events because of the finite diameter of the exit hole of the AT-TPC. Both of these acceptance losses were modeled in the simulations. For example, the acceptance of the ^{12}C fragment after population and decay of ^{13}C excited through the $^{13}\text{N}(d, ^2\text{He})^{13}\text{C}$ reaction is displayed as a function of excitation energy in ^{13}C in Fig. 7. The acceptance losses become significant at high excitation energies. In summary, because the acceptance is a function of ϵ_{pp} , $\theta_{c.m.}$, and the excitation energy of the $(d, ^2\text{He})$ reaction product, acceptance corrections were determined as a function of all three variables for the purpose of calculating differential cross sections.

E. Excitation energy spectra and differential cross sections

After the event selection, kinematic event reconstruction, and acceptance corrections, the excitation energy spectra and differential cross sections were calculated. The results are shown for the $^{13}\text{N}(d, ^2\text{He})$ and $^{14}\text{O}(d, ^2\text{He})$ reactions in Figs. 8(a) and 8(b), respectively. In both cases, the differential cross sections are shown for center-of-mass scattering angles between 0° and 8° , which constitutes the full angular range covered in the experiment. When the reaction Q value is near zero, the excitation energy primarily depends on the center-of-mass scattering angle of the ^2He system and the excitation-energy resolution is limited to $\approx 2.1 \text{ MeV}$. For ^{14}N , this happens at $E_x = 3.7 \text{ MeV}$, close to the excitation energy of the strong GT transition at 3.68 MeV . For ^{13}C , this occurs at $E_x = 0.77 \text{ MeV}$, close to the ground state. Away from $Q = 0$, the excitation energy depends on the center-of-mass scattering angle and the kinetic energy of the ^2He system, and the resolution that is achieved is $\approx 1.2 \text{ MeV}$.

The uncertainties in the cross sections include statistical uncertainties and systematic uncertainties. The latter are

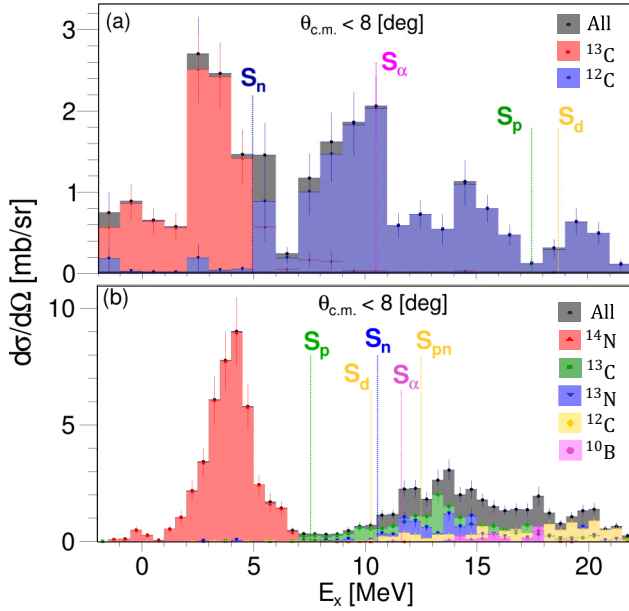


FIG. 8. Differential cross section for the (a) $^{13}\text{N}(d, ^2\text{He})$ and (b) $^{14}\text{O}(d, ^2\text{He})$ reactions for $\theta_{\text{c.m.}} \leq 8^\circ$. The dashed lines represent separation energies for different decay channels and the different colors indicate which residual particle was detected in the S800 spectrograph, as labeled in the figure. (a) shows differential cross section up to 22 MeV for the $^{13}\text{N}(d, ^2\text{He})$ reaction, but may have missing cross section above 17.5 MeV, which is the threshold for the decay by proton emission, as the ^{13}B fragment was not detected in the S800 spectrograph focal plane for the selected $B\rho$ settings.

dominated by uncertainties in the beam integration and the acceptance corrections for the two protons in the AT-TPC and the residual particles in the S800 spectrograph. Except for the strongly excited states at 3.68 MeV in ^{13}C and 3.95 MeV in ^{14}N , the statistical uncertainties are larger than the systematic uncertainties.

In both figures, the dashed lines indicate the thresholds for decay by particle emission, and the colors of the shaded regions indicate the residual particles measured in the focal plane of the S800 spectrograph. In the case of the $^{13}\text{N}(d, ^2\text{He})$ reaction, differential cross sections could be obtained up to an excitation energy of 17.5 MeV, which is the threshold for the decay by proton emission. Although the threshold for the decay by α -particle emission is only 10.6 MeV, only one event for was observed for ^9Be and was disregarded from the analysis. The threshold for the decay by deuteron emission is 18.7 MeV and beyond the excitation-energy range included in this analysis. In the case of the $^{14}\text{O}(d, ^2\text{He})$ reaction, differential cross sections up to an excitation energy of 22 MeV could be obtained, which required the inclusion of residual nuclei after the decay by neutron, proton, deuteron (or sequential emission of a neutron and a proton), and α -particle emission.

F. Multipole decomposition analysis

To extract the GT transition strength from the extracted differential cross sections, the $\Delta L = 0$ contribution must be isolated from the contributions associated with the transfer of

higher units of angular momentum transfer. This was done by performing a multipole decomposition analysis (MDA) [60,61], in which the measured differential cross sections are fitted with a linear combination of theoretically calculated differential cross sections associated with the transfer of different units of ΔL :

$$\left. \frac{d\sigma}{d\Omega}(\theta_{\text{c.m.}}) \right|_{\text{exp}} = a_0 \left. \frac{d\sigma}{d\Omega}(\theta_{\text{c.m.}}) \right|_{\Delta L=0} + a_1 \left. \frac{d\sigma}{d\Omega}(\theta_{\text{c.m.}}) \right|_{\Delta L=1} + a_2 \left. \frac{d\sigma}{d\Omega}(\theta_{\text{c.m.}}) \right|_{\Delta L=2}. \quad (6)$$

In this equation, a_i and $d\sigma/d\Omega(\theta_{\text{c.m.}})|_{\Delta L=i}$ (with $i = 0, 1, 2$) are the fit parameters and the theoretical angular distributions, respectively. We considered angular distribution for up to only $\Delta L = 2$ in the fit as the inclusion of terms with $\Delta L > 2$ did not improve the quality of the fit or impact the extracted $\Delta L = 0$ component. The theoretical calculations were performed with the ACCBA code (see Sec. III D). It is important to note that the differential cross sections presented in Fig. 8 are integrated over an ϵ_{pp} range that varies with scattering angle and excitation energy, as discussed in Sec. III D. This also means that, for a given excitation energy, the differential cross section as a function of scattering angle is biased by the ϵ_{pp} range that is within the acceptance of the experiment. Therefore, the theoretical angular distributions obtained from the ACCBA calculations were inserted in the ATTPCROOT simulation to account for the dependence of the ϵ_{pp} range on scattering angle and excitation energy prior to performing the MDA. This is illustrated in Fig. 9. Figure 9(a) shows the theoretical angular distributions for the $^{13}\text{N}(d, ^2\text{He})$ reaction (at an excitation energy of 3.68 MeV) for different units of ΔL . Figure 9(b) shows the angular distributions for each of the ΔL components after the acceptance for ϵ_{pp} has been accounted for. The differential cross section for the $\Delta L = 0$ calculation continues to peak at 0° , while those for $\Delta L = 1$ and $\Delta L = 2$ peak at finite angles. Each distribution is modified compared to the original angular distributions. Note that the acceptance for events with $\theta_{\text{c.m.}} < 0.25^\circ$ is near zero because the kinetic energy of the recoil ^2He is so low that either or both of the protons do not exit the central insensitive region of the AT-TPC, as shown in Fig. 6. Therefore, the angular range below $\theta_{\text{c.m.}} < 0.25^\circ$ was excluded from further analysis.

The MDA results for the $^{14}\text{O}(d, ^2\text{He})$ reaction were detailed in Ref. [28]. The results for the MDA for the $^{13}\text{N}(d, ^2\text{He})$ reaction are shown in Fig. 10. Compared to the case of ^{14}O , the statistical uncertainties in the ^{13}N data are significantly larger, simply due to the difference in beam intensity for the two beams in the cocktail beam. Therefore, an MDA of the excitation energy spectrum on a bin-by-bin basis was not feasible and, for the purpose of the MDA, the spectrum was divided in four different regions, as shown in Fig. 10.

The first region corresponds to the population of the transition from the $^{13}\text{N}(1/2^-)$ g.s. to the $^{13}\text{C}(1/2^-)$ g.s.. As discussed above, this transition can be associated with ($\Delta S = 1$) and without ($\Delta S = 0$) the transfer of spin. However, the ($d, ^2\text{He}$) reaction selects transitions with $\Delta S = 1$ and the cross section is dominated by the GT transition strength of $B(\text{GT}) =$

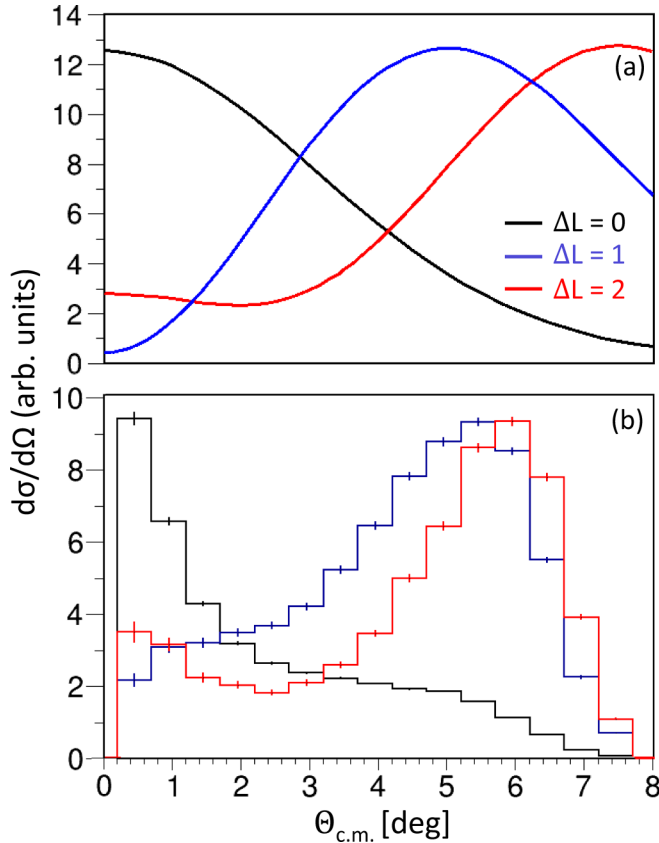


FIG. 9. Calculated differential cross section as a function of center-of-mass scattering angle for $\Delta L = 0, 1,$ and 2 components for the $^{13}\text{N}(d, ^2\text{He})$ reaction at an excitation energy of 3.68 MeV in ^{13}C . (a) shows the differential cross sections obtained directly from the ACCBA code. (b) shows the differential cross section obtained after accounting for the ϵ_{pp} acceptance by using the ATTPCROOT simulation code. Note that in this plot, the error bars are indicative of the statistical uncertainties in the Monte Carlo simulations. Also note that the differential cross sections in both plots have been scaled so that their maxima are approximately identical for visualization purposes.

0.207 ± 0.002 deduced from the $\log ft$ value of 3.6648 from β decay [32]. The MDA of Fig. 10(a) indicates that the transition is dominated by $\Delta L = 0$, as expected.

The second region, between excitation energies of 2 MeV and 6 MeV, is known to have several positive-parity states, but also contains the transition to the $3/2^-$ state at 3.68 MeV, which is of interest for the astrophysical purposes discussed in Sec. I. Similar to the results from the analog $^{13}\text{C}(p, n)$ and $^{13}\text{C}(^3\text{He}, t)$ experiments, the excitation of this state is dominant in this region, given that the MDA indicates that the cross section is almost entirely due to the $\Delta L = 0$ excitation, as shown in Fig. 10(b).

The third region, between excitation energies of 7 MeV and 12 MeV, is known to have numerous states. Based on the $^{13}\text{C}(^3\text{He}, t)$ data, at least four GT transitions to states in this region exist. With the statistics available in the present experiment, an MDA is only possible for the region as a

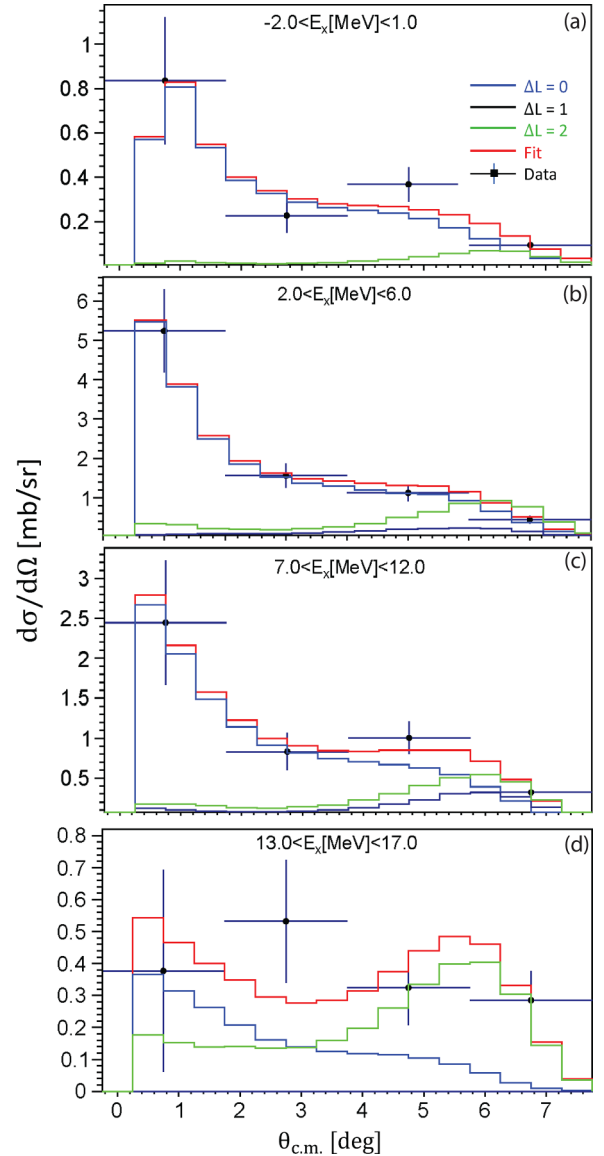


FIG. 10. MDA results for different ranges in excitation energy, as discussed in the text.

whole, as shown in Fig. 10(c), indicating a significant amount of $\Delta L = 0$ strength associated with these GT transitions.

Finally, the region around the known $3/2^-, T = 3/2$ state at 15.1 MeV state was investigated by using the MDA, as shown in Fig. 10(d). The statistical uncertainties are particularly large in this region, but the results suggest a significant $\Delta L = 0$ component associated with the population of the 15.1 MeV state.

G. Extraction of GT strengths

To extract the GT strengths from the differential cross sections for the $\Delta L = 0$ contributions in the MDA, the differential cross sections were extrapolated to values at zero momentum transfer ($q = 0$) and $\epsilon_{pp} < 1$ MeV on the basis of the ACCBA calculations. This also makes it possible to compare the extracted unit cross sections from the present

TABLE I. Comparison of $B(\text{GT})$ values extracted from the $^{13}\text{N}(d, ^2\text{He})$ reaction, the $^{13}\text{C}(^3\text{He}, t)$ [31,40] reaction, β decay data, and shell-model calculations with the CKII interaction.

$^{13}\text{N}(d, ^2\text{He})$		$^{13}\text{C}(^3\text{He}, t)$ [31,40]		β decay		Shell Model CKII ^a	
E_x (^{13}C) (MeV)	$B(\text{GT})$	E_x (^{13}N) (MeV)	$B(\text{GT})$	E_x (MeV)	$B(\text{GT})$	E_x (MeV)	$B(\text{GT})$
0	0.27 ± 0.07	0	–	0	0.207 ± 0.002	0	0.193
2–6	1.37^{b}	3.51	1.37 ± 0.07	–	–	3.69	1.52
7–12	0.93 ± 0.23	7–12	0.93 ± 0.05	–	–	7–12	0.70
–	–	8.92	0.27 ± 0.02	–	–	8.65	0.39
–	–	9.48	0.06 ± 0.01	–	–	–	–
–	–	10.83	0.11 ± 0.01	–	–	10.63	0.31
–	–	11.88	0.48 ± 0.04	–	–	–	–
13–17	0.19 ± 0.15	–	0.23	–	–	–	0.30
–	–	–	–	–	–	13.83	0.07
–	–	15.06	0.23^{c}	–	$0.23 \pm 0.01^{\text{d}}$	14.68	0.23

^aAfter multiplying with a phenomenological quenching factor of 0.68 [35].

^bFixed to $B(\text{GT})$ from the analog transition excited via $^{13}\text{C}(^3\text{He}, t)$ reaction [31] as described in the text.

^cFixed to the value from β decay.

^dDeduced from analog β -decay transitions from the g.s. of ^{13}B to the g.s. of ^{13}C and from the g.s. of ^{13}O to the g.s. of ^{13}N [13,31].

experiment with the value of $\hat{\sigma} = 2.58 \pm 0.14$ mb/sr obtained for the $^{12}\text{C}(d, ^2\text{He})$ reaction performed in forward kinematics at an incident energy of $E_d = 170$ MeV [21]. As discussed in Ref. [41], for the transition to the 3.95-MeV state in ^{14}N through the $^{14}\text{O}(d, ^2\text{He})$ reaction, a unit cross section of $\hat{\sigma} = 2.74 \pm 0.29$ mb/sr was extracted, consistent with the earlier result. Here we focus on the strength and unit cross section extraction for the $^{13}\text{N}(d, ^2\text{He})$ reaction.

IV. RESULTS AND DISCUSSION

The unit cross section for the $^{13}\text{N}(d, ^2\text{He})$ reaction could be calibrated using any of the three transitions: to the g.s., to the 3.68 MeV state, or to the 15.1 MeV state. For those to the g.s. and to the 15.1 MeV state, the $B(\text{GT})$ values are known from β decay or through isospin-symmetry considerations, respectively. Unfortunately, the statistical uncertainties associated with these two transitions in the present analysis are large. In order to minimize the impact of the limited statistics available for the present experiments, we therefore used the extracted $B(\text{GT})$ from the $^{13}\text{C}(^3\text{He}, t)$ experiments for the transition to the analog of the 3.68 MeV state (with a $B(\text{GT})$ of 1.37 ± 0.07 [31]) to extract the unit cross section for the present experiment and then compare consistency with GT strengths obtained in the other excitation-energy regions. After extrapolating to $q = 0$ and $\epsilon_{pp} < 1$ MeV on the basis of the ACCBA calculations, the unit cross section was found to be 2.62 ± 0.36 mb/sr, which is consistent with the values found for the $^{14}\text{O}(d, ^2\text{He})$ reaction from this experiment and the value found previously for the $^{12}\text{C}(d, ^2\text{He})$ reaction [21].

The results for the extracted GT strengths in all regions of the excitation-energy spectrum of ^{13}C listed above are presented in Table I and compared with the results from the $^{13}\text{C}(^3\text{He}, t)$ analysis [31,40] and the shell-model calculations utilizing the CKII interaction described above. The comparison is also presented in Fig. 11. For the $B(\text{GT})$ values for transitions to states between 7 MeV and 12 MeV via the

$^{13}\text{C}(^3\text{He}, t)$ reaction, the data from Ref. [40] were calibrated using the transition to the 15.1 MeV state to establish the unit cross section, in the same manner as in Ref. [31].

Overall, it is found that the results from the $^{13}\text{N}(d, ^2\text{He})$ measurements are consistent with those from the $^{13}\text{C}(^3\text{He}, t)$ experiments. The shell-model calculations provide a reasonable representation of the experimental data, after applying the phenomenological quenching factor, although a complete correspondence between transitions observed in the experiments and calculated in the shell model cannot be made at higher excitation energies.

Although it is helpful to confirm that the results from the $^{13}\text{N}(d, ^2\text{He})$ experiment are consistent with the results from the $^{13}\text{C}(^3\text{He}, t)$ experiments, due to the limited statistics available for the present data, it is not possible to improve on the precision for the inputs for the astrophysical calculations for EC rates on ^{13}N presented in Ref. [31]. On the other hand,

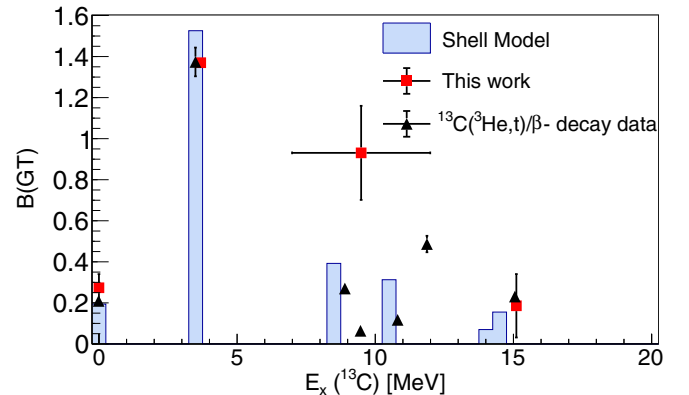


FIG. 11. Comparison of the extracted GT strengths from the $^{13}\text{N}(d, ^2\text{He})$ reaction with shell model calculations using the CKII interaction in the p -shell-model space, and strengths extracted for the analog $^{13}\text{C}(^3\text{He}, t)$ reaction, calibrated with β -decay data [31,40].

it is clear that constraints on GT strengths provided by the ($d, {}^2\text{He}$) reaction in inverse kinematics will be important for probing nuclei further away from stability, where no data from analog transitions in forward kinematics experiments with high-intensity light-ion beams will be available. Given that the ${}^{13}\text{N}$ beam intensity during the experiment ranged between 23 kpps and 161 kpps, it is reasonable to assume that an intensity of about 100 kpps is a lower limit for the extraction of GT strengths of about 0.1 within several days of beam time with the current technique. We remind the reader that the results for the ${}^{14}\text{O}(d, {}^2\text{He})$ reaction are detailed in Ref. [28]. The more detailed comparison with *ab initio* coupled-cluster and shell-model calculations benefited from about three times more beam intensity than available for the ${}^{13}\text{N}(d, {}^2\text{He})$ data. Besides beam intensity, other factors play a role. The differential cross sections for ($d, {}^2\text{He}$) reactions drop with increasing mass number. On the other hand, the loss of events due to the limited size of the exit hole in the AT-TPC and acceptance of the spectrograph will reduce when performing experiments in inverse kinematics with heavier beams, as the momentum kicks induced through the decay(s) by particle emission will be reduced. Finally, the relative differences in $B\rho$ between residual nuclei produced in the decay by particle emission of the fast charge-exchange product reduce when performing experiments with heavier nuclei, reducing the number of $B\rho$ settings required to obtain the spectra up to high excitation energies.

V. SUMMARY AND OUTLOOK

The ($d, {}^2\text{He}$) reaction in inverse kinematics has been developed as a novel tool for extracting GT transition strengths up to high excitation energies from unstable nuclei in the β^+/EC direction. The development is important for constraining EC rates in stellar environments. This technique could be used to either constrain particular individual rates, such as the EC on ${}^{13}\text{N}$ described in this paper, or benchmark theoretical models that aim to estimate EC rates on a wide range of nuclei that play roles in astrophysical processes. Prior to the development

of the ($d, {}^2\text{He}$) reaction in inverse kinematics, no experimental technique was available to achieve the same purpose.

To perform the ($d, {}^2\text{He}$) experiment in inverse kinematics, the AT-TPC was utilized in combination with the S800 spectrograph. The combination of the two devices ensures a very clean selection of ($d, {}^2\text{He}$) events and identification of the decay channel, if the residual particle is created beyond the particle-separation threshold. The use of a gaseous target, necessary for detecting and characterizing the two low-energy protons created in the ($d, {}^2\text{He}$) reaction at low momentum transfers, requires that beam intensities of about 100 kpps or more are available to identify GT transitions with strengths of 0.1. In the experiment described in this work, beam intensities reached 700 kpps. Given the availability of high-intensity beams for nuclei relatively far from stability at existing and future state-of-the-art rare-isotope beam facilities, the prospects for expanding the use of the ($d, {}^2\text{He}$) reaction in inverse kinematics are bright.

ACKNOWLEDGMENTS

We thank all the staff at NSCL for their support. This work was supported by the US National Science Foundation under Grants No. PHY-1913554 (Windows on the Universe: Nuclear Astrophysics at the NSCL), No. PHY-2209429, “Windows on the Universe: Nuclear Astrophysics at FRIB”, No. PHY-1430152 (JINA Center for the Evolution of the Elements), and No. PHY-1927130 (AccelNet-WOU: International Research Network for Nuclear Astrophysics [IReNA]). The AT-TPC was partially funded by the US National Science Foundation under Grant No. MRI-0923087. This material is also based upon work supported by the U.S. Department of Energy, Office of Science, Office of Nuclear Physics and used resources of the Facility for Rare Isotope Beams (FRIB), which is a DOE Office of Science User Facility, operated by Michigan State University, under Award No. DE-SC0000661. S.N.B. would like to acknowledge Grants No. RYC2020-030669 and No. PID2022-142557NA-I00 funded by MCIN/AEI/10.13039/501100011033 for travel support.

-
- [1] H. A. Bethe, *Rev. Mod. Phys.* **62**, 801 (1990).
 - [2] H. A. Bethe, G. E. Brown, J. Applegate, and J. M. Lattimer, *Nucl. Phys. A* **324**, 487 (1979).
 - [3] G. M. Fuller, W. A. Fowler, and M. J. Newman, *Astrophys. J. Suppl. Series* **48**, 279 (1982).
 - [4] P. Haensel and J. L. Zdunik, *Astron. & Astrophys.* **227**, 431 (1990).
 - [5] K. Iwamoto, F. Brachwitz, K. Nomoto, N. Kishimoto, H. Umeda, W. R. Hix, and F. Thielemann, *Astrophys. J. Suppl. Series* **125**, 439 (1999).
 - [6] F. Brachwitz, D. J. Dean, W. R. Hix, K. Iwamoto, K. Langanke, G. Martínez-Pinedo, K. Nomoto, M. R. Strayer, F. Thielemann, and H. Umeda, *Astrophys. J.* **536**, 934 (2000).
 - [7] H. Janka, K. Langanke, A. Marek, G. Martínez-Pinedo, and B. Müller, *Phys. Rep.* **442**, 38 (2007).
 - [8] H. Schatz, S. Gupta, P. Möller, M. Beard, E. F. Brown, A. T. Deibel, L. R. Gasques, W. R. Hix, L. Keek, R. Lau *et al.*, *Nature (London)* **505**, 62 (2014).
 - [9] C. L. Doherty, P. Gil-Pons, L. Siess, and J. C. Lattanzio, *Publ. Astron. Soc. Aust.* **34**, e056 (2017).
 - [10] K. Langanke, G. Martínez-Pinedo, and R. G. T. Zegers, *Rep. Prog. Phys.* **84**, 066301 (2021).
 - [11] J. Cooperstein and J. Wambach, *Nucl. Phys. A* **420**, 591 (1984).
 - [12] K. Langanke and G. Martínez-Pinedo, *Nucl. Phys. A* **673**, 481 (2000).
 - [13] T. N. Taddeucci, C. A. Goulding, T. A. Carey, R. C. Byrd, C. D. Goodman, C. Gaarde, J. Larsen, D. Horen, J. Rapaport, and E. Sugarbaker, *Nucl. Phys. A* **469**, 125 (1987).

- [14] R. G. T. Zegers, R. Meharchand, Y. Shimbara, S. M. Austin, D. Bazin, B. A. Brown, C. A. Diget, A. Gade, C. J. Guess, M. Hausmann *et al.*, *Phys. Rev. Lett.* **104**, 212504 (2010).
- [15] R. Meharchand, R. G. T. Zegers, B. A. Brown, S. M. Austin, T. Baugher, D. Bazin, J. Deaven, A. Gade, G. F. Grinyer, C. J. Guess, M. E. Howard, H. Iwasaki, S. McDaniel, K. Meierbachtol, G. Perdikakis, J. Pereira, A. M. Prinke, A. Ratkiewicz, A. Signoracci, S. Stroberg *et al.*, *Phys. Rev. Lett.* **108**, 122501 (2012).
- [16] H. Ohnuma, K. Hatanaka, S. I. Hayakawa, M. Hosaka, T. Ichihara, S. Ishida, S. Kato, T. Niizeki, M. Ohura, H. Okamura *et al.*, *Phys. Rev. C* **47**, 648 (1993).
- [17] H. Okamura, S. Fujita, Y. Hara, K. Hatanaka, T. Ichihara, S. Ishida, K. Katoh, T. Niizeki, H. Ohnuma, H. Otsu, H. Sakai, N. Sakamoto, Y. Satou, T. Uesaka, T. Wakasa, and T. Yamashita, *Phys. Lett. B* **345**, 1 (1995).
- [18] H. Okamura, T. Uesaka, K. Suda, H. Kumasaka, R. Suzuki, A. Tamii, N. Sakamoto, and H. Sakai, *Phys. Rev. C* **66**, 054602 (2002).
- [19] H. M. Xu, G. K. Ajupova, A. C. Betker, C. A. Gagliardi, B. Kokenge, Y.-W. Lui, and A. F. Zaruba, *Phys. Rev. C* **52**, R1161 (1995).
- [20] D. Frekers and M. Alanssari, *Eur. Phys. J. A* **54**, 177 (2018).
- [21] S. Rakers, F. Ellinghaus, R. Bassini, C. Bäumer, A. van den Berg, D. Frekers, D. De Frenne, M. Hagemann, V. Hannen, M. Harakeh, M. Hartig, R. Henderson, J. Heyse, M. de Huu, E. Jacobs, M. Mielke, J. Schippers, R. Schmidt, S. van der Werf, and H. Wörtche, *Nucl. Instrum. Meth. Phys. Res. A* **481**, 253 (2002).
- [22] C. Bäumer, A. M. van den Berg, B. Davids, D. Frekers, D. De Frenne, E.-W. Grewe, P. Haefner, M. N. Harakeh, F. Hofmann, M. Hunyadi, E. Jacobs, B. C. Junk, A. Korff, K. Langanke, G. Martínez-Pinedo, A. Negret, P. von Neumann-Cosel, L. Popescu, S. Rakers, A. Richter *et al.*, *Phys. Rev. C* **68**, 031303(R) (2003).
- [23] C. Bäumer, A. M. van den Berg, B. Davids, D. Frekers, D. De Frenne, E.-W. Grewe, P. Haefner, M. N. Harakeh, F. Hofmann, S. Hollstein, M. Hunyadi, M. A. de Huu, E. Jacobs, B. C. Junk, A. Korff, K. Langanke, G. Martínez-Pinedo, A. Negret, P. von Neumann-Cosel, L. Popescu *et al.*, *Phys. Rev. C* **71**, 024603 (2005).
- [24] M. Hagemann, A. van den Berg, D. De Frenne, V. Hannen, M. Harakeh, J. Heyse, M. de Huu, E. Jacobs, K. Langanke, G. Martínez-Pinedo, and H. Wörtche, *Phys. Lett. B* **579**, 251 (2004).
- [25] M. Hagemann, C. Bäumer, A. M. van den Berg, D. De Frenne, D. Frekers, V. M. Hannen, M. N. Harakeh, J. Heyse, M. A. de Huu, E. Jacobs, K. Langanke, G. Martínez-Pinedo, A. Negret, L. Popescu, S. Rakers, R. Schmidt, and H. J. Wörtche, *Phys. Rev. C* **71**, 014606 (2005).
- [26] L. Popescu, C. Bäumer, A. M. van den Berg, D. Frekers, D. De Frenne, Y. Fujita, E. W. Grewe, P. Haefner, M. N. Harakeh, M. Hunyadi, M. A. d. Huu, E. Jacobs, H. Johansson, A. Korff, A. Negret, P. v. Neumann-Cosel, S. Rakers, A. Richter, N. Ryezayeva, A. Shevchenko *et al.*, *Phys. Rev. C* **75**, 054312 (2007).
- [27] E.-W. Grewe, C. Bäumer, H. Dohmann, D. Frekers, M. N. Harakeh, S. Hollstein, H. Johansson, K. Langanke, G. Martínez-Pinedo, F. Nowacki, I. Petermann, L. Popescu, S. Rakers, D. Savran, K. Sieja, H. Simon, J. H. Thies, A. M. van den Berg, H. J. Wörtche, and A. Zilges, *Phys. Rev. C* **77**, 064303 (2008).
- [28] S. Giraud, J. C. Zamora, R. G. T. Zegers, D. Bazin, Y. Ayyad, S. Bacca, S. Beceiro-Novo, B. A. Brown, A. Carls, J. Chen, M. Cortesi, M. DeNudt, G. Hagen, C. Hultquist, C. Maher, W. Mittig, F. Ndayisabye, S. Noji, S. J. Novario, J. Pereira *et al.*, *Phys. Rev. Lett.* **130**, 232301 (2023).
- [29] S. Kox, J. Carbonell, C. Furget, T. Motobayashi, C. Perrin, C. Wilkin, J. Arvieux, J. Bocquet, A. Boudard, G. Gaillard *et al.*, *Nucl. Phys. A* **556**, 621 (1993).
- [30] D. A. Chamulak, E. F. Brown, F. X. Timmes, and K. Dupczak, *Astrophys. J.* **677**, 160 (2008).
- [31] R. G. T. Zegers, E. F. Brown, H. Akimune, S. M. Austin, A. M. van den Berg, B. A. Brown, Y. Chamulak, D. A. Fujita, M. Fujiwara, S. Galés, M. N. Harakeh, H. Hashimoto, R. Hayami, G. W. Hitt, M. Itoh, T. Kawabata, K. Kawase, M. Kinoshita, K. Nakanishi, S. Nakayama, S. Okamura *et al.*, *Phys. Rev. C* **77**, 024307 (2008).
- [32] F. Ajzenberg-Selove, *Nucl. Phys. A* **523**, 1 (1991).
- [33] B.A. Brown *et al.*, OXBASH, Report 524, MSU-NSCL, 1985.
- [34] S. Cohen and D. Kurath, *Nucl. Phys.* **73**, 1 (1965).
- [35] W.-T. Chou, E. K. Warburton, and B. A. Brown, *Phys. Rev. C* **47**, 163 (1993).
- [36] X. Wang, J. Rapaport, M. Palarczyk, C. Hautala, X. Yang, D. L. Prout, I. Van Heerden, R. Howes, S. Parks, E. Sugarbaker, and B. A. Brown, *Phys. Rev. C* **63**, 024608 (2001).
- [37] E. K. Warburton and B. A. Brown, *Phys. Rev. C* **46**, 923 (1992).
- [38] T. N. Taddeucci, J. Rapaport, D. E. Bainum, C. D. Goodman, C. C. Foster, C. Gaarde, J. Larsen, C. A. Goulding, D. J. Horen, T. Masterson, and E. Sugarbaker, *Phys. Rev. C* **25**, 1094(R) (1982).
- [39] C. D. Goodman, R. C. Byrd, I. J. van Heerden, T. A. Carey, D. J. Horen, J. S. Larsen, C. Gaarde, J. Rapaport, T. P. Welch, E. Sugarbaker, and T. N. Taddeucci, *Phys. Rev. Lett.* **54**, 877 (1985).
- [40] H. Fujimura, H. Akimune, I. Daito, M. Fujiwara, K. Hara, K. Y. Hara, M. N. Harakeh, F. Ihara, T. Inomata, K. Ishibashi, T. Ishikawa, T. Kawabata, A. Tamii, M. Tanaka, H. Toyokawa, T. Yamanaka, and M. Yosoi, *Phys. Rev. C* **69**, 064327 (2004).
- [41] S. Giraud, J. Zamora, R. Zegers, Y. Ayyad, D. Bazin, W. Mittig, A. Carls, M. DeNudt, and Z. Rahman, *Nucl. Instrum. Meth. Phys. Res. A* **1051**, 168213 (2023).
- [42] D. Morrissey, B. Sherrill, M. Steiner, A. Stolz, and I. Wiedenhoever, *Nucl. Instrum. Methods Phys. Res. Sect. B* **204**, 90 (2003), 14th International Conference on Electromagnetic Isotope Separators and Techniques Related to their Applications.
- [43] D. Bazin, J. Caggiano, B. Sherrill, J. Yurkon, and A. Zeller, *Nucl. Instrum. Methods Phys. Res. Sect. B* **204**, 629 (2003), 14th International Conference on Electromagnetic Isotope Separators and Techniques Related to their Applications.
- [44] J. Bradt, D. Bazin, F. Abu-Nimeh, T. Ahn, Y. Ayyad, S. Beceiro Novo, L. Carpenter, M. Cortesi, M. P. Kuchera, W. G. Lynch, W. Mittig, S. Rost, N. Watwood, and J. Yurkon, *Nucl. Instrum. Meth. Phys. Res. A* **875**, 65 (2017).
- [45] J. Yurkon, D. Bazin, W. Benenson, D. Morrissey, B. Sherrill, D. Swan, and R. Swanson, *Nucl. Instrum. Meth. Phys. Res. A* **422**, 291 (1999).
- [46] Y. Ayyad, W. Mittig, D. Bazin, S. Beceiro-Novo, and M. Cortesi, *Nucl. Instrum. Meth. Phys. Res. A* **880**, 166 (2018).
- [47] J. Zamora and G. Fortino, *Nucl. Instrum. Meth. Phys. Res. A* **988**, 164899 (2021).

- [48] J. F. Ziegler, M. Ziegler, and J. Biersack, *Nucl. Instrum. Methods Phys. Res. Sect. B* **268**, 1818 (2010), 19th International Conference on Ion Beam Analysis.
- [49] Y. Ayyad, W. Mittig, D. Bazin, and M. Cortesi, *J. Phys.: Conf. Ser.* **876**, 012003 (2017).
- [50] Y. Ayyad, ATTPCROOT, <https://github.com/ATTPC/ATTPCROOTv2> (2022).
- [51] H. Okamura, *Phys. Rev. C* **60**, 064602 (1999).
- [52] B. Brown and W. Rae, *Nucl. Data Sheets* **120**, 115 (2014).
- [53] M. A. Hofstee, S. Y. van der Werf, A. M. van den Berg, N. Blasi, J. A. Bordewijk, W. T. A. Borghols, R. De Leo, G. T. Emery, S. Fortier, S. Galès, M. N. Harakeh, P. den Heijer, C. W. de Jager, H. Langevin-Joliot, S. Micheletti, M. Morlet, M. Pignanelli, J. M. Schippers, H. de Vries, A. Willis, and A. van der Woude, *Nucl. Phys. A* **588**, 729 (1995).
- [54] S. Y. van der Werf, computer program NORMOD (unpublished).
- [55] W. G. Love and M. A. Franey, *Phys. Rev. C* **24**, 1073 (1981).
- [56] M. A. Franey and W. G. Love, *Phys. Rev. C* **31**, 488 (1985).
- [57] A. Koning and J. Delaroche, *Nucl. Phys. A* **713**, 231 (2003).
- [58] A. J. Koning, S. Hilaire, and M. C. Duijvestijn, in *International Conference on Nuclear Data for Science and Technology* (EPJ, Les Ulis, 2007), pp. 211–214.
- [59] A. Koning and D. Rochman, *Nucl. Data Sheets* **113**, 2841 (2012).
- [60] B. Bonin, N. Alamanos, B. Berthier, G. Bruge, H. Faraggi, D. Legrand, J. Lugol, W. Mittig, L. Papineau, A. Yavin *et al.*, *Nucl. Phys. A* **430**, 349 (1984).
- [61] M. Moinester, A. Trudel, K. Raywood, S. Yen, B. Spicer, R. Abegg, W. Alford, N. Auerbach, A. Celler, D. Frekers *et al.*, *Phys. Lett. B* **230**, 41 (1989).